Matching Traffic Demand in GEO Multibeam Satellites: The Joint Use of Dynamic Beamforming and Precoding Under Practical Constraints

Haythem Chaker, *Graduate Student Member, IEEE*, Houcine Chougrani, Wallace A. Martins, *Senior Member, IEEE*, Symeon Chatzinotas, *Senior Member, IEEE*, and Joel Grotz, *Member, IEEE*

***Abstract*—To adjust for the non-uniform spatiotemporal nature of traffic patterns, next-generation high throughput satellite (HTS) systems can benefit from recent technological advancements in the space-segment in order to dynamically design traffic-adaptive beam layout plans (ABLPs). In this work, we propose a framework for dynamic beamforming (DBF) optimization and adaptation in dynamic environments. Given realistic traffic patterns and a limited power budget, we propose a feasible DBF operation for a geostationary multibeam HTS network. The goal is to minimize the mismatch between the traffic demand and the offered capacity under practical constraints. These constraints are dictated by the traffic-aware design requirements, the on-board antenna system limitations, and the signaling considerations in the K-band. Noting that the ABLP is agnostic about the inherent inter-beam interference (IBI), we construct an interference simulation environment using irregularly shaped beams for a large-scale multibeam HTS system. To cope with IBI, the combination of on-board DBF and on-ground precoding is considered. For precoded and non-precoded HTS configurations, the proposed design shows better traffic-matching capabilities in comparison to a regular beam layout plan. Lastly, we provide trade-off analyses between system-level key performance indicators for different realistic non-uniform traffic patterns.**

***Index Terms*—Dynamic beamforming, flexible GEO satellite, inter beam interference, realistic non-uniform traffic demand.**

I. Introduction

While spectrum and power resources remain scarce, modern broadband services provided by satellite communication (SatCom) systems are expanding, thus causing an unprecedented growth in data traffic demand. Moreover, the user-link demand distributions (traffic patterns) are significantly varying across different service areas and during different time instances [1].

Manuscript received 19 February 2022; revised 6 July 2022; accepted 23 July 2022. Date of publication 17 August 2022; date of current version 9 December 2022. This work was supported by the Luxembourg National Research Fund (FNR) through the Frame of the Research Project "Dynamic Beam Forming and In-Band Signalling for Next Generation Satellite Systems" (DISBuS) under Grant BRIDGES19/IS/13778945/DISBuS. *(Corresponding author: Haythem Chaker.)*

Haythem Chaker, Houcine Chougrani, Wallace A. Martins, and Symeon Chatzinotas are with the Interdisciplinary Centre for Security, Reliability and Trust, University of Luxembourg, 1511 Luxembourg City, Luxembourg (e-mail: haythem.chaker@uni.lu).

Joel Grotz is with SES, 6815 Betzdorf, Luxembourg.

Digital Object Identifier 10.1109/TBC.2022.3196173

In high throughput satellite (HTS) systems, the payload covers service areas using multiple beams in order to increase its user-link total offered throughput (TOT) [2]. As a conventional radio resource management (RRM) strategy, typical in-orbit payloads use a static regular beam layout plan (RBLP), a four-frequency reuse (4FR) scheme, and a uniform per-beam power allocation to illuminate the coverage area where user terminals (UTs) are expected to be located. However, given the heterogeneous nature of the traffic patterns, some beams can exhaust the aggregate user-link offered throughput, causing an increase in per-beam and system-unmet capacities (BUC/SUC). On the other hand, underused beams can witness considerable per-beam and duly system-excess capacities (BEC/SEC). These mismatches translate into a waste of system resources and a loss of revenues for the satellite operators.

In response to this, the broadband SatCom market anticipates the introduction of flexible payloads — in the sense of traffic-adaptive RRM and transmission techniques — in order to enhance the users' quality of service (QoS) and to reduce the cost per bit in future HTS systems. In the space-segment, digital on-board processors (OBP) together with large-scale active antennas (LSAA) emerge as the preferred technological enablers related to these goals [3]. SES's next-generation of in-orbit programmable satellite systems [4] are an example.

In this context, this paper thoroughly investigates upcoming processed and LSAA-based satellite architectures from a system-level [5] to a user-level point of view for different non-uniform traffic patterns. The main idea is to dynamically adapt the beam layout in order to maximize the system's traffic matching performance by exploiting the reconfigurable capabilities of next-generation payloads. The latter is done taking into account practical constraints such as the limited on-board power budget, payload mass and size, and signaling regulations in the K-band.

A. Related Works

In practice, the performance of any space-segment beamforming design heavily relies on the traffic pattern, i.e., the disperse geographic location information of the UTs in the service areas and their corresponding data demand. The traffic demand is readily accessible at the network hub (see, for instance, [6], [7]), whereas the users' spatiotemporal

distributions can be reliably estimated through the satellite ephemeris and the geospatial coordinates of the UT population. It is therefore possible to target a traffic-adaptive beamforming design that defines the number [8], positions [9], [10], [11], and shapes [12], [13] of the beams, i.e., the *beam layout*. The aforementioned works focus on circular beam shapes, as they allow to model closed-form beam layout plans (BLPs) [14], [15] ensuring global coverage [16], docile inter-beam interference (IBI) [17], and a simple multibeam antenna system design.

Moreover, encouraging research on precoding for flexible payloads are reported in [18] and in [19] for geosynchronous orbit (GEO) and medium Earth orbit (MEO) HTS systems, respectively. In these findings, relevant increase in the system's TOT is shown for a hot-spot scenario with 7 beams given a uniform user distribution. Herein, nonetheless, we will focus on a whole system coverage area (similar to [20]), resulting in a more complete large-scale HTS system performance evaluation. Other relevant traffic-adaptive precoding algorithms for SatCom can be found in [21], [22].

Given the particularly non-uniform QoS requirements, devising optimization methodologies for such large-scale problems, with novel constraints upon on-board resources, computation and spectrum sharing, poses significant challenges to the emerging payloads. In this context, the search space of optimal (traffic-adaptive) system parameters is too large and a high degree of flexibility typically entails NP-hard [23] or non-convex formulations [6]. This fact is also common in precoded HTS systems [22], which in addition necessitate a channel estimation procedure. Subsequently, different sub-optimal paradigms with different degrees of flexibilities arise; see for example [24] and references therein.

Recent works in SatCom utilize heuristics (e.g., [12], [23], [25]) or learning based (e.g., [7], [26]) techniques to optimize certain flexibilities of the multibeam traffic-matching problem. In particular, authors in [26] propose an adaptive beam layout plan (ABLP) solution using a clustering method on the coverage area. The approach uses traffic demand and location information of the users to obtain a satisfactory uniform distribution of the demand across beams with elliptic shapes.

For a given non-uniform traffic pattern, the ABLP solution is not unique. Moreover, different ABLPs with different constraints can be envisaged in a dynamic beamforming (DBF) framework. For example, the ABLP method from [26] uses an elliptic Gaussian beam footprint model featuring no sidelobes. Using this supposition, the radio-frequency (RF) coverage area *inside* a given beam is smoothly filled with no nulls. As a result, a preliminary traffic matching performance is produced at the expense of ignoring IBI outside the beam. We tackle this problem by introducing a gain/directivity control operation in the DBF framework considering practical constraints.

Another concern is that precoding increases the computational burden of the system [27]. With this in mind, a tangible scaling of each degree of freedom, at different traffic patterns, is still missing in litterature. Therefore, we consider realistic non-uniform traffic patterns on an hourly basis [1]. Using accurate IBI modeling, we also evaluate performance and trade-off between DBF and non-DBF HTS system configurations featuring different precoding algorithms.

B. Contribution

This work focuses on sizing the attainable flexibility extent of emerging payloads. Under practical constraints, the traffic-matching performance is evaluated by quantifying beam and system, unmet and excess capacities (UC/EC). This is done for different configurations featuring the juxtaposition of DBF and precoding. In order to build a traffic and link conditioned network in the forward-link, we primarily propose a DBF optimization framework before applying different precoders.

Modeling all the radio resource dependencies and the multiple interconnecting constraints across variables is prohibitive. Therefore, we assume the necessary system-level simplifications to build a realistic and tractable *interference-limited* physical (PHY) channel environment. This allows to evaluate generic payload and network architectures under the imposed requirements. On these grounds, we approach a sequential structure in this work in order to show the importance of DBF and higher frequency reuse orders on the overall system design trade-off. Hence, the contributions of this work are as follows:

1) Generic Radiation Model for Shaped Beams: To model the high directivity of generic HTS front-end (e.g., different LSAA technologies that are capable of generating shaped beams) as well as to tractably express payload constraints, we employ the expressions of the *ITU-R.672 general co-polar model 2* ([28, Sec. 2.4.2]). To the best of our knowledge, this contribution stands as the first academic work that takes this complex radiation model into account. We show how to *design shaped beams* and diagnose systematic HTS/DBF dependencies, without loss of generality.

2) Feasible Coverage Adaptability: We study the physical feasibility and necessary resource planning for the target DBF design in [26]. We also extend its adaptability under a limited power-budget. This constitutes the main DBF optimization framework: where we assume the initial ABLP for a particular traffic scenario to be valid, and we analytically express a two-dimensional (2D) beamwidth flexibility under system design, payload and signaling constraints.

3) IBI Management: Once the IBI PHY environments are built for different system settings (i.e., ABLPs and RBLP), for each traffic profile, we evaluate the traffic matching performances with 4FR and full frequency reuse (FFR). Concerning FFR, we use schemes of the minimum mean square error (MMSE) precoder [29] and the weighted max-min (w-MM) signal-to-interference-plus-noise-ratio (SINR) precoder [21]. We initially assume that channel state information (CSI) is ideally available at the gateway at transmission; before we stress the practical performance under non-perfect CSI estimation conditions. The DVB-S2X [30] data rates and a practical CSI estimation error model [31], [32] are used.

C. Paper Organization

Section II details the traffic and system models. Section III explores the proposed DBF optimization framework. In

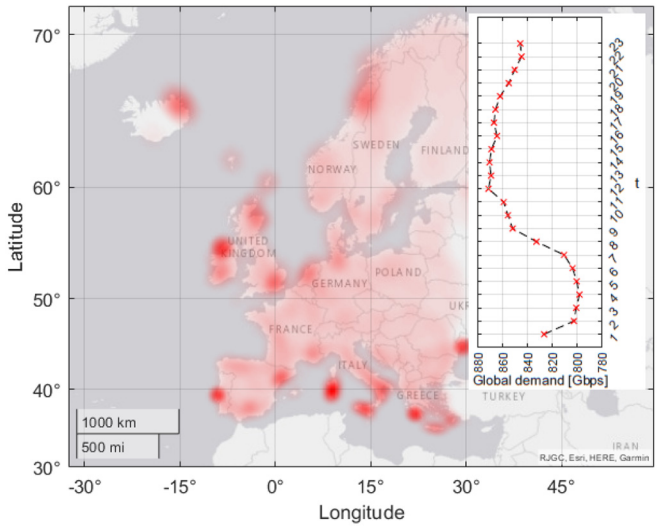

Fig. 1. Spatial demand density of an emulated traffic pattern over Europe (from [1] at 12h) featuring fixed and mobile UTs of different classes. Hot-spots are highlighted with a darker color while cold-spots with lighter ones.

Section IV, IBI management is elaborated. In Section V, traffic matching performance evaluation and trade-off are discussed for different system configurations and for different traffic patterns. Conclusions are drawn in Section VI.

Notations: Respectively, $(\bullet)^T$, $(\bullet)^\dagger$, $\odot$ and $\oslash$ denote the transpose operator, the conjugate transpose operator, the Hadamard product and the Hadamard division. The Frobenius norm is denoted by $\|\bullet\|$, while $\mathbf{1}_K$ is the $K \times 1$ all-one vector. The boundary of a geometric area E is denoted with ∂E.

II. Traffic and System Models

An ABLP approximately satisfies a uniform distribution of the traffic demand using irregularly shaped beams (e.g., see the ABLPs in [15] and [26]). In this work, we aim to design the beams with irregular shapes. This operation is possible given the high number of radiating elements in LSAA, which can form highly directive beampatterns. The DBF-operation follows an ABLP by means of digital processing. Moreover, the DBF-operation is executed using an up-to-date ABLP each time a significant shift in the traffic pattern occurs.

With DBF, however, the non-deterministic features of traffic patterns can yield ABLPs with intractably overlapping beams. This potentially causes excessive IBI for ABLPs as compared to RBLPs. Before addressing DBF and IBI, we present in this section the considered traffic and system models.

A. Traffic Model

We focus on the use case of adapting an HTS network to the non-uniform spatiotemporal variations of traffic of different user classes. Hourly volatile traffic patterns are obtained using a traffic emulator (TE) [1] where the disperse geographic and time statistics reflect different realistic data sources of fixed, maritime, and aerial users. We showcase in Fig. 1 the traffic spatial distribution at the peak global traffic demand scenario.

Using the TE, at observation t, a user j requests a traffic $D_j^{(t)}$ in bit per second (bps). The traffic *profile* of a given BLP with K beams is designated by a vector $\widetilde{\boldsymbol{D}}^{(t)} \in \mathbb{R}_{\geq 0}^{K\times 1}, \forall t$, of *average* aggregate traffic demands per-beam as defined in [5]. The analyses in the sequel apply to any BLP using the PHY model presented in the next section.

B. System Model

Consider the K-band forward-link of a GEO HTS network having a fully programmable payload equipped with LSAA. We precisely focus on the user-link performance for a single gateway with an ideal feeder-link unless otherwise specified. The geostationary satellite occupies the orbital position (R_s, ρ_s, ϕ_s) in the geographic coordinate system (GCS). We express $R_s = \mathrm{R_E} + r_s$ in meters, where $\mathrm{R_E} = 6871\,\mathrm{km}$ is Earth's mean radius and $r_s > 0$ is the GEO satellite altitude.

All users are assumed to have an identical single antenna UT equipment with a receiver gain $G_{\mathrm{RX}} > 0$. The user positions are mapped on a discrete grid over the Earth with a resolution that determines the granularity of the longitude and latitude coordinates (ρ_m, ϕ_m). The slant range from the satellite to a user located at point m is calculated in meters using

$$r_m = \Big\{R_s^2 + \mathrm{R_E^2} - 2R_s\mathrm{R_E}(\cos\phi_m \cos\phi_s \cos(\rho_s - \rho_m) + \sin(\phi_s\phi_m))\Big\}^{\frac{1}{2}}. \quad (1)$$

The payload is assumed to have a single antenna aperture $A > 0$ in meters. It covers a continuous geographic areas by illuminating Earth's surface with a number $K > 0$ of potentially overlapping beams. The beams denoted $k \in \mathcal{K} = \{1, \ldots, K\}$ are arranged according to a particular BLP.

Using the DVB-S2X frame [30], let us consider a time division multiplexed (TDM) unicast transmission of independent signals intended for simultaneously scheduled users. For each traffic profile, we can then assume a single super-user per-beam $u \in \mathcal{K}$ that encompasses each beam's *average* aggregate traffic demand, i.e., $D_u \triangleq [\widetilde{\boldsymbol{D}}]_k, \forall u \in \mathcal{K}$. We note that at each independent frame realization, the selected users can have different coordinates (ρ_u, ϕ_u) and slant ranges $[\boldsymbol{r}]_u = r_u$ populating a vector $\boldsymbol{r} \in \mathbb{R}_{>0}^{K\times 1}$.

We represent by $\boldsymbol{x} \in \mathbb{C}^{K\times 1}$ the vector of the transmitted symbols, and by $\boldsymbol{n} \in \mathbb{C}^{K\times 1}$ the independent and identically distributed (i.i.d.) received noise samples $[\boldsymbol{n}]_u \sim \mathcal{CN}(0, P_{\mathrm{n}})$, where $P_{\mathrm{n}} > 0$ is the noise power. Taking independent random channel observations, the fixed multibeam channel coefficients $[\boldsymbol{H}]_{u,k}$ between the u-th user and the k-th beam footprint are expressed in the matrix $\boldsymbol{H} \in \mathbb{C}^{K\times K}$ written as

$$\boldsymbol{H} = \sqrt{\boldsymbol{G}} \odot \widetilde{\boldsymbol{H}}. \quad (2)$$

In (2), $\boldsymbol{G} \in \mathbb{R}^{K\times K}$ is the beam gain matrix further elaborated in Section III-A, and $\widetilde{\boldsymbol{H}} \in \mathbb{C}^{K\times K}$ is a matrix encompassing the link-budget factors. The link is considered to be line-of-sight with no multi-path effects. We designate by $\lambda = \frac{f_0}{c}$ the free-space wavelength, by f_0 the carrier frequency and by c the speed of light. Furthermore, let the diagonal matrix $\boldsymbol{\Psi} \in \mathbb{R}^{K\times K}$ have elements $[\boldsymbol{\Psi}]_{k,k}$ denoting the user-related signal phase rotations that are i.i.d. at each t [5]. In addition, let $P_{\mathrm{L}} > 0$ represent the slow-fading losses of the user-link RF channel

(including rain attenuation) exhibited at each beam footprint, and experienced by each of the UT antennas. We then have

$$\widetilde{\boldsymbol{H}} = \sqrt{\frac{G_{\mathrm{RX}}}{P_{\mathrm{n}} P_{\mathrm{L}}}} \frac{\lambda}{4\pi} \left(\boldsymbol{I}_K \oslash \boldsymbol{r}^T\right) \odot \exp\left(\imath \, \frac{2\pi}{\lambda} \left(\boldsymbol{I}_K \odot \boldsymbol{r}^T\right) + \boldsymbol{\Psi}\right). \quad (3)$$

Depending on the RRM configuration, the signals from the beam footprints received at the UT antennas can cause co-channel IBI and are expressed in the vector $\boldsymbol{y} \in \mathbb{C}^{K\times 1}$ using

$$\boldsymbol{y} = \boldsymbol{H}\boldsymbol{x} + \boldsymbol{n}. \quad (4)$$

III. Dynamic Beamforming Framework

We refer by DBF the ability of an HTS to adjust the linear combination of the on-board LSAA beampatterns to match the template beampatterns of a BLP. This operation is the central role of the on-board beamforming network (BFN) and it highly depends on the technologies and architecture involved. Generally, DBF can be analog, digital or hybrid (both analog and digital) depending on payload resources, complexity and other coverage/satellite parameters. In this section we present the building blocks of the proposed DBF optimization framework for a practical traffic-adaptive and large-scale HTS system, given a limited power-budget.

A. Generic Radiation Model for Shaped Beams

We start by introducing the flexibility notions for our DBF optimization framework. In fact, since the lobed behavior of an antenna system of any HTS is unduly sensitive to the UT position, the beam gain matrix $\boldsymbol{G}$ is typically derived from the array factor of the payload's antenna system in the far field and the users' positions. In the following, we present a suitable abstraction for $\boldsymbol{G}$ in order to enable comparisons between (precoded and non-precoded) RBLPs and ABLPs regardless of specific antenna array or BFN characteristics. More precisely, to evaluate the performance of DBF in HTS, we require a reliable modeling of the radiation response for i) multiple ii) shaped beams iii) including their sidelobes' behavior as a function of the shape. The requirement iii) is particularly important to evaluate the interference sensitive systems, especially in the case of FFR.

In particular, we employ a generic *design objective* beam radiation model, namely the *ITU-R.672 general co-polar model 2* (see [28, Sec. 2.4.2]). The model provides a general antenna radiation mask, which can describe DBF-based applications. The model takes into account design requirements, theoretical considerations, physical impairments and introduces different parameters to describe them (e.g., scan ratio, beam broadening factor, illumination law, etc.). In the Appendix, we present a detailed description of the model's expressions (41) and parameters (see Table III) whereas the corresponding reference template of the model is depicted in Fig. 2.

To understand the relevence of the selected model for highly directive LSAA, let us first assume a one-to-one correspondence between the k-th beam and the k-th service zone of interest (ZOI). The k-th ZOI is defined by a convex polygon Z_k in the satellite-centered coordinate system (CCS).[1] In addition, for a given ZOI, we define its unique minimum area circumscribing ellipse [26], [34], i.e., *the beamlet* B_k, which will be used as reference in beamforming design.

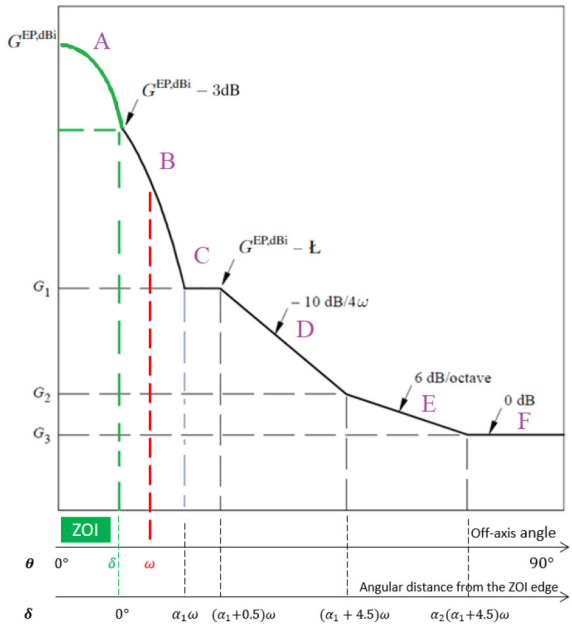

Fig. 2. The reference radiation mask regions reproduced from the ITU-R. 672 general co-polar model 2 [28] expressed in (41) in the Appendix.

Rigorously, for a beam k, let $\tau_k \in [0°, 90°[$ be the tilt angle of a beamlet's major axis w.r.t. the off bore-sight angle φ_k expressed as $\varphi_k = \arctan(\frac{r_k}{R_s}) > 0$. A beamlet B_k can then be parameterized by $B_k \leftrightsquigarrow (\varphi_k, \theta_{\mathrm{A}|k}, \theta_{\mathrm{B}|k}, \tau_k)$, where the angular distances $\theta_{\mathrm{B}|k} > 0°$ and $\theta_{\mathrm{A}|k} \geq \theta_{\mathrm{B}|k}$ respectively correspond to the semi-minor and the semi-major axes of the minimum circumscribing ellipse of the k-th ZOI Z_k.

Note that one way to model a QoS guarantee is to design an RF beam to have a 3 dB level below its equivalent peak (EP) gain at all the polygonal sides of its ZOI. Using the ITU-R model, Z_k and B_k are utilized to determine the directivity of the k-th beam by considering the 2D widths $(\theta_{\mathrm{A}|k}, \theta_{\mathrm{B}|k})$ to be comparable to the ones of a regular elliptic beam (defined by its 2D 3 dB beamwidths). In fact, the directivity of a "conservative elliptic beam k" determines the shape of its beampattern and its isotropic EP gain at the mainlobe axis:

$$G_k^{\mathrm{EP,dBi}} = 10 \log_{10}\left(\frac{\eta(\pi\kappa)^2}{\theta_{\mathrm{A}|k}\theta_{\mathrm{B}|k}}\right), \quad (5)$$

expressed in dBi, with η corresponding to the satellite antenna efficiency term, and κ to the diffraction limit factor [5].

It is clear from the expressions in (41) (see Fig. 2) that the directional beam gain is inversely proportional to the user's angular distance from the beam center. For the user u and

[1] For BLP, in order to conserves the shape of the beams, it is ordinary to use a projection map from the GCS made on a plane which is at right-angles to the satellite-Earth vector, namely the CCS Cartesian plane $(\theta\cos(\varphi), \theta\sin(\varphi))$ centered with a nadir pointing at the intersection of the zero-meridian and the equator (ρ_0, ϕ_0). Coordinate system transformations can be found in [33].

beam k, the beam gain coefficient can then be calculated using

$$[\boldsymbol{G}]_{u,k} = \text{anti-log}\left\{G^{\text{dBi}}(u,k)\right\} \triangleq 10^{\frac{G^{\text{dBi}}(u,k)}{10}}. \tag{6}$$

Before explaining how each ZOI is obtained in the next sections, we highlight herein relevant key parameters intrinsic to the model. We denote by Ł $\gg 3$ dB the target near-in-sidelobe discrimination level relative to $G_k^{\text{EP,dBi}}$ and required by the HTS design for all the beams, and by $G1 = G_k^{\text{EP,dBi}} - Ł$ (the peak) sidelobes plateau in dB. In addition, let the scalar

$$\alpha_{2|k} \triangleq \text{anti-log}\left\{\frac{G_k^{\text{EP,dBi}} - Ł - 10}{2}\right\} \tag{7}$$

represent a design parameter that is relative to the shape degradation effects of the beam, which are dominated by the reflection and diffraction phenomena at the aperture edge (see Appendix). The expressions presented in this section will be used in the proposed DBF optimization framework.

B. Traffic-Aware Coverage Adaptability

In this work, the flexible payload is assumed to illuminate a coverage area through its single antenna aperture A using the combination of K beam footprints. We recall that a DBF-operation designates the application of the design objective radiation model presented in Section III-A on a set $\mathcal{Z} = \bigcup_{k\in\mathcal{K}} Z_k$ corresponding to K target ZOIs representing a BLP.

Notice that for a set $\mathcal{Z}$ describing a BLP, a set $\mathcal{B} = \bigcup_{k\in\mathcal{K}} B_k$ of K beamlets with precise 2D beamwidths is defined. For RBLPs, it is possible to use only $\mathcal{B}$ to shape the beams such that each ZOI Z_k is simplified to be equal to its corresponding b_k, at the step of applying the radiation model. Note that, in general, for an elliptic beamlet b_k, $\omega(\cdot,k)$ (see Appendix) varies between $\theta_{\text{B}|k}$ and $\theta_{\text{A}|k}$, and that for a circular Z_i definition, i.e., $Z_k = b_k$, we have $\omega(\cdot,k) = \delta(\cdot,k) = \theta_{\text{A}|k} = \theta_{\text{B}|k}$; hence the unidimensional regular beamwidth definition found in RBLPs.

As for an ABLP case, we apply the presented radiation model using the combination of both the ZOI and the beamlet of each beam, at the DBF-operation. This is possible through the introduction of $\delta(m,k), \forall(m,k)$, in the model expressions (see Appendix). Whereas, in this case, the role of the beamlets $\mathcal{B}$ is limited to referencing the EP gain (5) and the radial distances ω. The output superimposed targeted beampatterns are sharply shaped according to the 3 dB contours of the ZOI from $\mathcal{Z}$ (where each beam can have a different size and shape), hence the high directivity of the DBF-operation.

From the relationship in (5), we assess that a beamlet's gain is inversely proportional to its (3 dB) service area. This means that the wider a beam, the lower its gain and vice-versa. Even though the actual offered throughput per-beam largely depends on the allocated bandwidth and power, the latter feature is empowered in this traffic-aware coverage adaptability step of the DBF-operation to serve hot-spot service zones with higher gains and cold-spot service zones (see Fig. 1) with lower gains.

Specifically, we extend the ABLP from [26] that follows a learning method based on the traffic patterns (e.g., from [1]), to cluster the RF coverage area (as seen from the CCS) into a set $\mathcal{Z}$ of adjacent and non-overlapping convex polygons. Such a tessellation of the service area of interest guarantees the absence of non covered areas. The clustering objective is to uniformly balance the total system traffic demand distribution across the K ZOI in order to obtain a fair system performance. A system (i.e., $SX10$, 1 for DBF on, 0 for unfeasible) implementing such a fairness-ABLP is the *initial target beampattern design*. Such a system is proven to reduce the BUC and BEC; hence it increases the system's demand matching capabilities.

Notably, DBF comes with limitations related to the BFN architecture, the OBP capabilities, and the LSAA geometry as well as the limited on-board resources. In the following, we exploit the radiation model expression to study the feasibility of a DBF-operation concertizing a feasible ABLP, and to compare its performance to a benchmark system with a static RBLP (i.e., $SX0$, 0 for DBF off).

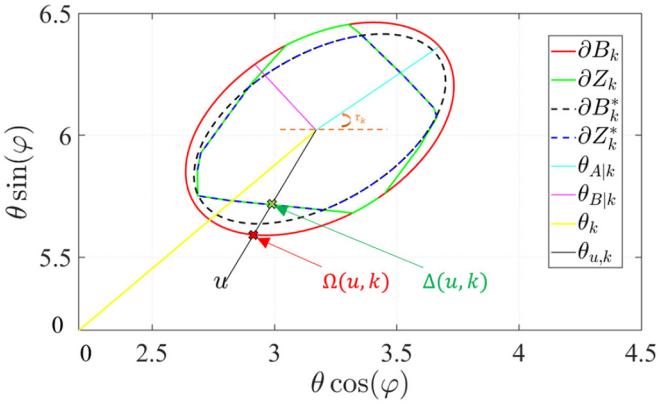

Fig. 3. The geometries defining a ZOI (in green) and its corresponding beamlet (in red), its optimized feasible solution (in dashed blue), and the reference optimized beamlet (in dashed black), as well as the angular relations to an arbitrary user u. The operators Δ and Ω are explained in the Appendix.

C. Shaping Feasible Beams

Note that for a feasible ZOI, i.e., Z_k^*, the RF coverage *shape* is defined using its 3 dB contour ∂Z_k^*. The corresponding optimized reference beamlet B_k^* has a direct impact on the EP gain and the beampattern as discussed above. We can further characterize this using

$$\partial Z_k^* = \partial Z_k \bigcap \partial B_k^*. \tag{8}$$

For a user u, the different geometries w.r.t. a k-th ZOI and its corresponding beamlet are depicted in Fig. 3.

For each beam k, we keep the coverage strengths of the ABLP (the tilt angles τ_k are fixed) and its traffic adaptability strengths (by locking the beam positions to obtain maximum directivity at the center of each ZOI, i.e., θ_k is initialized as the centroid of the corresponding k-th ZOI). We are then remained with 2D beamwidth flexibilities to utilize in the design of feasible beams as will be elaborated in the next sections.

We remind that we want to contrast a conventional payload utilizing an RBLP ($SX0$ with a fixed EP gain $G_{\text{RBLP}}^{\text{EP}}$) versus a DBF-capable payload with an ABLP (i.e., with dynamic EP gains at each beam). Therefore, it is worthwhile mentioning

that assuming a same transmission power P per-beam, different effective equivalent isotropic radiated power (EIRP) levels can be obtained. This can bias the performance comparison, hence an EIRP equalization [5] is needed for each beam k:

$$\mathrm{EIRP}_{\mathrm{RBLP}} = \mathrm{EIRP}_{\mathrm{ABLP}} \tag{9a}$$

$$\implies P_{\mathrm{ABLP}} = P_{\mathrm{RBLP}}, \frac{G^{\mathrm{EP}}_{\mathrm{RBLP}}}{G^{\mathrm{EP}}_{k}}, \tag{9b}$$

$$\implies G^{\mathrm{EP},*}_{k} = P_{\mathrm{RBLP}} \frac{G^{\mathrm{EP}}_{\mathrm{RBLP}}}{\max\limits_{m\in\partial Z^*} G(m,k)}. \tag{9c}$$

D. Beam Gain Control Under Practical Considerations

Revisiting the definition of a beamlet B_k as a best fit ellipse approximation of a convex ZOI Z_k, we recall that the centroid of the ZOI and of the center of the corresponding beamlet would coincide. From (5) and (8), this means that the EP gain of a feasible elliptic beamlet $B^*_k = (\varphi_k, \theta^*_{\mathrm{A}|k}, \theta^*_{\mathrm{B}|k}, \tau_k)$ lower bounds the EP of the shaped beam Z^*.

For a beam k having an initially targeted beamlet (in $SX10$) with axes $(\theta^{\mathrm{init}}_{\mathrm{A}|k}, \theta^{\mathrm{init}}_{\mathrm{B}|k})$, consider the problem formulation in $\mathcal{P}^{(1)}$ where the 2D "beamwidth flexibility" obeys system specific constraints:

$$\mathcal{P}^{(1)}\colon \underset{\theta_{\mathrm{A}},\theta_{\mathrm{B}}}{\text{minimize}} \ \sqrt{\left(\theta_{\mathrm{A}} - \theta^{\mathrm{init}}_{\mathrm{A}}\right)^2 + \left(\theta_{\mathrm{B}} - \theta^{\mathrm{init}}_{\mathrm{B}}\right)^2}$$

$$\text{subject to} \quad G^{\min} \le G^{\mathrm{EP}}(\theta_{\mathrm{A}}, \theta_{\mathrm{B}}) \tag{10a}$$

$$\theta^{\min} \le \theta_{\mathrm{A}} \tag{10b}$$

$$\theta^{\min} \le \theta_{\mathrm{B}} \tag{10c}$$

$$1 \le \frac{\theta_{\mathrm{A}}}{\theta_{\mathrm{B}}} \tag{10d}$$

$$\frac{\theta_{\mathrm{A}}}{\theta_{\mathrm{B}}} < \alpha_2. \tag{10e}$$

In $\mathcal{P}^{(1)}$, notice that we dropped the subscript for the beamwidths. This is because $\mathcal{P}^{(1)}$ is a *beam by beam gain control optimization* under a fixed power allocation assumption per-beam (see Section III-C). We next detail the design of DBF systems with feasible beampatterns (i.e., $SX11$, the first digit (1) designates DBF on, and the second one (1) indicates a practical solution using $\mathcal{P}^{(1)}$).

In constraint (10a), in compliance with spectrum sharing radio regulations (RR) [35] in the K-band, we derive the minimum gain (maximum beamwidths) bound at the edge of beam k, i.e., supporting a QoS gain guarantee above -3 dB w.r.t. the EP gain, namely

$$\hat{G}^{\mathrm{min,dB}}_{k} = \text{anti-log}\left\{\mathrm{EIRP}^{\mathrm{max,dB}}_{k} - \hat{P}^{\mathrm{dB}} - 3\,\mathrm{dB}\right\}. \tag{11}$$

In (11), $\hat{G}^{\min}_{k} > 0, \forall k$, and the maximum allowed EIRP at the beam center is expressed in decibel as [35]

$$\mathrm{EIRP}^{\mathrm{max,dB}}_{k} = \mathrm{PFD}^{\max}(\epsilon_k) + 10\log_{10}\left(4\pi r_k^2\right). \tag{12}$$

Moreover, $\hat{P}^{\mathrm{dB}} = 10\log_{10}(\hat{P})$ is the power initialization seed which we assume uniformly equal for all beams in this step: i.e., $P^{\mathrm{tot}} = K\hat{P} > 0$ is the total available transmission power. According to ITU-R SF.358-5 [36], the maximum allowed power flux density (PFD), i.e., $\mathrm{PFD}^{\max}$, is expressed in dB(W/m^2) in function of ϵ_k the angle of elevation above the horizon. This angle is calculated for a point m using $\epsilon_m = \arccos(\frac{R_s}{\sin(\varphi_m)})$ [33].

To derive the maximum gain (minimum beamwidth) bound, we consider the same sine illumination function used in the ITU-R.672 model, where for each beamlet, a circular aperture (for maximum gain) with an edge taper of -4 dB is assumed. With this simplification, we fix $G1 = 16.56$ dB [37] as the first sidelobe peak and $\frac{\alpha_1}{2} \approx 0.775$ considering a typical symmetric first-sidelobe target Ł $= 20$ dB w.r.t. the maximum allowed EP gain. In this case, in order to guarantee a sufficient discrimination between close ZOI with an Ł level below their EP gains, each beamlet has beamwidth θ_{A} (and respectively θ_{B}) lower bounded by [28]

$$\theta^{\min} = (16.56 + 0.775Ł)\frac{\lambda}{A}, \tag{13}$$

as modeled in the constraints in (10b) and (10c). The relationship in (13) allows to respect considerations relative to the operating frequency, the payload's mass and size (using the value of A), in addition to the designed discriminate first sidelobe limit[2] Ł. Furthermore, one strength of the generic radiation model is that a generalization of the aperture shape is possible through the payload specific enhancement parameters detailed in Table III in the Appendix.

Having respectively introduced a signaling constraint (10a) and two design constraints (10b) and (10c), a minimum and a maximum ellipticity requirements are derived from the angular beamwidth limits of equations (41). From regions B and C corresponding to $0° \le \delta(m,k) \ (\alpha_1 + 0.5)\omega(m,k)$ in (41) (see Fig. 2), a unitary minimum ellipticity term $(\frac{\alpha_1}{\alpha_1} = 1)$ yields a circular beam at the limit, i.e., constraint (10d). While from regions E and F corresponding to $(\alpha_1 + 4.5)\omega(m,k) \le \delta(m,k) \le 90°$ in (41), let $X > \frac{\alpha_1+0.5}{\alpha_1}$ distinguish the maximum ellipticity term as explicated below.

For clarity, we rearrange $\mathcal{P}^{(1)}$ using the relationship (9c) and the expression of α_2 from (7), such that

$$\mathcal{P}^{(1)}\colon \underset{\theta_{\mathrm{A}},\theta_{\mathrm{B}}}{\text{minimize}} \ \sqrt{\left(\theta_{\mathrm{A}} - \theta^{\mathrm{init}}_{\mathrm{A}}\right)^2 + \left(\theta_{\mathrm{B}} - \theta^{\mathrm{init}}_{\mathrm{B}}\right)^2}$$

$$\text{subject to} \quad Y\theta_{\mathrm{A}}\theta_{\mathrm{B}} \le 1 \tag{14a}$$

$$\theta^3_{\mathrm{A}} - X\theta_{\mathrm{B}} < 0 \tag{14b}$$

$$\theta^{\min} - \theta_{\mathrm{A}} \le 0 \tag{14c}$$

$$\theta_{\mathrm{B}} - \theta_{\mathrm{A}} \le 0. \tag{14d}$$

For the k-th beam, the two derived scalar quantities

$$X \triangleq \exp\left(\ln\left(\eta(\pi\kappa)^2\right) - \ln(10)\left(\frac{Ł}{10} + 1\right)\right), \tag{15}$$

$$Y_k \triangleq \frac{\eta(\pi\kappa)^2}{\hat{G}^{\min}_{k}}, \tag{16}$$

[2]According to ITU-R [28], the recommended range for Ł is [20, 30] dB for interference sensitive systems. We verified numerically that for an extreme Ł $= 20$ dB (assumed in (13)), three narrow beams sharing the user-link spectrum in FFR and co-interfering at a common point do obey the maximum allowed PFD regulation [35], [36] in the K-band. The GEO HTS system specifications used are detailed in Section V.

respectively represent the maximum ellipticity term induced by reflective effects in the wide-angle sidelobe (region F corresponding to $(\alpha_1 + 4.5)\omega(m,k) \leq \delta(m,k) < (\alpha_1 + 4.5)\alpha_2\omega(m,k)$ in (41)), and the maximum *feasible* effective solid angle given a power allocation assumption as in (11).

Problem $\mathcal{P}^{(1)}$ is convex for $\theta^{\min} \leq \theta_{\mathrm{B}} \leq \theta_{\mathrm{A}}$ except for constraint (14a). We propose to approximate this minimum gain constraint using the initially designed beamwidth information by replacing it with

$$\theta_{\mathrm{B}} - \left(\frac{-Y}{\left(\theta_{\mathrm{A}}^{\mathrm{init}}\right)^2} \left(\theta_{\mathrm{A}} - \theta_{\mathrm{A}}^{\mathrm{init}}\right) - \frac{Y}{\theta_{\mathrm{A}}^{\mathrm{init}}} \right) \leq 0. \tag{17}$$

Adjusting the beamlet's beamwidths this way guarantees a feasible system $SX11$ assuming a uniform beam power initialization. As shown in the next section, dropping the latter assumption for more flexibility, it is possible to jointly optimize the beamwidths for practical considerations and to derive the necessary power budget P^{tot} given a target ABLP.

E. Directivity Control Under Practical Considerations

Let us now consider the joint design of K feasible beams given their corresponding initial beamlets in $\mathcal{B}$. We can then define $\boldsymbol{\theta}_{\mathrm{A}}^{\mathrm{init}} = [\theta_{\mathrm{A}|1}^{\mathrm{init}} \dots \theta_{\mathrm{A}|K}^{\mathrm{init}}]^T \in \mathbb{R}_+^{K\times 1}$ and $\boldsymbol{\theta}_{\mathrm{B}}^{\mathrm{init}} = [\theta_{\mathrm{B}|1}^{\mathrm{init}} \dots \theta_{\mathrm{B}|K}^{\mathrm{init}}]^T \in \mathbb{R}_+^{K\times 1}$ as two vectors containing the initially planned beamwidths. In addition, let $\boldsymbol{p} = [p_1 \dots p_K]^T \in \mathbb{R}_+^{K\times 1}$ be a vector designating the minimum per-beam required power, such that $P^{\mathrm{tot},*} = \prod_{k=1}^{K} [\boldsymbol{p}^*]_k$ is the minimum power budget required to achieve feasible beams. In the same fashion as the previous section, the feasibility of the beams is designed using the constraints formulated in problem $\mathcal{P}^{(2)}$:

$$\mathcal{P}^{(2)}\colon \underset{\boldsymbol{\theta}_{\mathrm{A}},\boldsymbol{\theta}_{\mathrm{B}},\boldsymbol{p}}{\text{minimize}} \quad \sum_{k=1}^{K} \sqrt{\left([\boldsymbol{\theta}_{\mathrm{A}}]_k - \left[\boldsymbol{\theta}_{\mathrm{A}}^{\mathrm{init}}\right]_k\right)^2 + \left([\boldsymbol{\theta}_{\mathrm{B}}]_k - \left[\boldsymbol{\theta}_{\mathrm{B}}^{\mathrm{init}}\right]_k\right)^2}$$

$$\text{subject to} \quad [\boldsymbol{\theta}_{\mathrm{B}}]_k - \left([\boldsymbol{Z}_1]_k \left([\boldsymbol{\theta}_{\mathrm{A}}]_k - \left[\boldsymbol{\theta}_{\mathrm{A}}^{\mathrm{init}}\right]_k\right) - [\boldsymbol{Z}_0]_k\right) \leq 0 \tag{18a}$$

$$[\boldsymbol{\theta}_{\mathrm{A}}]_k^3 - X[\boldsymbol{\theta}_{\mathrm{B}}]_k < 0 \tag{18b}$$

$$\theta^{\min} - [\boldsymbol{\theta}_{\mathrm{A}}]_k \leq 0 \tag{18c}$$

$$[\boldsymbol{\theta}_{\mathrm{B}}]_k - [\boldsymbol{\theta}_{\mathrm{A}}]_k \leq 0 \tag{18d}$$

$$0 < [\boldsymbol{p}]_k \tag{18e}$$

$$\boldsymbol{p} \odot \text{anti-log}(\boldsymbol{G}^{\min,\mathrm{dB}}) \leq \mathrm{EIRP}^{\max}, \tag{18f}$$

The constraints (18b)-(18d) are respectively analogous to constraints (14b)-(14d) of $\mathcal{P}^{(1)}$ in K dimensions. Similarly, a vectorized form of the approximated (equation (17)) minimum gain constraint is in (18a), where the vectors $\boldsymbol{Z}_1 \triangleq -\boldsymbol{Y} \oslash (\boldsymbol{\theta}_{\mathrm{A}}^{\mathrm{init}} \odot \boldsymbol{\theta}_{\mathrm{A}}^{\mathrm{init}}) \in \mathbb{R}^{K\times 1}$ and $\boldsymbol{Z}_0 \triangleq \boldsymbol{Y} \oslash \boldsymbol{\theta}_{\mathrm{A}}^{\mathrm{init}} \in \mathbb{R}^{K\times 1}$ serve for expressive brevity. We also define the vectors $\boldsymbol{Y} \triangleq (\eta(\pi\kappa)^2)\mathbf{1}_K \oslash \boldsymbol{G}^{\min}) \in \mathbb{R}^{K\times 1}$, $\boldsymbol{G}^{\min} \triangleq \text{anti-log}(\boldsymbol{G}^{\min,\mathrm{dB}})$, $\boldsymbol{G}^{\min,\mathrm{dB}} \triangleq \mathrm{EIRP}^{\max,\mathrm{dB}} - \hat{\boldsymbol{p}}^{\mathrm{dB}} - 3\,\mathrm{dB}$ and $\mathrm{EIRP}^{\max} \in \mathbb{R}^{K\times 1}$. In particular, $\mathrm{EIRP}^{\max}$ is the vector representing the maximum permissible EIRP for each beam in resemblance to the anti-log of (12), given the initial power seed vector $\hat{\boldsymbol{p}}^{\mathrm{dB}} = 10\log_{10}(\hat{P})\mathbf{1}_K \in \mathbb{R}^{K\times 1}$. For the last two constraints in $\mathcal{P}^{(2)}$, (18e) allocates a non-zero power to each beam. While (18f) equalizes the transmitted power jointly during the 2D beamwidth optimization.

Problem $\mathcal{P}^{(2)}$ is convex and it defines a feasible system ($SX12$, 1 for DBF on, 2 for solution of problem $\mathcal{P}^{(2)}$). This parallel DBF design executes K times faster than the gain control design in $\mathcal{P}^{(1)}$. In fact, the joint optimization on gain and power gives the optimization in $\mathcal{P}^{(2)}$ a *directivity control* character in the feasibility sense.

On another hand, for a given initial target ABLP, i.e., $\mathcal{B}$, the derived minimum power budget $P^{\mathrm{tot},*}$ should belong to a feasible power pool such that $\hat{P} \leq P^{\mathrm{tot},*} \leq P^{\max}$, with $P^{\max}$ being the available transmit at the payload. This power constraint is critical to determine the feasibility of an ABLP in a power-stressed system. Using this approach, for any IBI management strategy, we fix the common power budget P^{tot} necessary for the DBF and non-DBF HTS systems.

IV. IBI Management

To cope with IBI, for both RBLPs and ABLPs, we summarize in this section the considered precoding algorithms.

At this stage, we note the DBF and the precoding technologies do not operate on the same time-scale. On the one hand, precoding adapts the signals on a frame basis based on the selected set of users. And on the other hand, DBF is executed on a longer time-scale based on the traffic evolution.

A. Precoding With Ideal CSI Estimation

In precoding, the full frequency band of the user-link $\mathrm{B}_0 > 0$ is aggressively reused among the scheduled users. We therefore refer to a division of B_0 by a number of colors $N_{\mathrm{c}}^{\mathrm{FFR}} = 1$. Assuming the CSI in (2) is ideally available at the gateway, the transmitted signals $\boldsymbol{x}$ are constructed through a linear combination of the i.i.d. information symbols elements of vector $\boldsymbol{s} \in \mathbb{C}^{K\times 1}$, using a precoding matrix $\boldsymbol{Q} \in \mathbb{C}^{K\times K}$ such that $\boldsymbol{x} = \boldsymbol{Q}\boldsymbol{s}$.

Let $\boldsymbol{q}_u \in \mathbb{C}^{K\times 1}$ be the u-th column of $\boldsymbol{Q}$. The linear multibeam channel equation in (4) becomes $\boldsymbol{y} = \boldsymbol{H}\boldsymbol{Q}\boldsymbol{s} + \boldsymbol{n}$. The resulting received signal by user u whose corresponding channel is $\boldsymbol{h}_u \in \mathbb{C}^{K\times 1}$ being the u-th row of $\boldsymbol{H}$, is

$$\begin{aligned} y_u &= \boldsymbol{h}_u^{\dagger}\boldsymbol{Q}\boldsymbol{s} + [\boldsymbol{n}]_u \\ &= \boldsymbol{h}_u^{\dagger}\boldsymbol{q}_u[\boldsymbol{s}]_u + \sum_{j\in\mathcal{K}\setminus\{u\}} \boldsymbol{h}_u^{\dagger}\boldsymbol{q}_j[\boldsymbol{s}]_j + [\boldsymbol{n}]_u. \end{aligned} \tag{19}$$

Assuming $\mathbb{E}\{[\boldsymbol{s}]_u\} \sim \mathcal{CN}(0,1)$ in the remainder, the total transmitted power at any instance is then given by

$$\|\boldsymbol{Q}\|^2 = \sum_{u=1}^{K} \|\boldsymbol{q}_u\|^2. \tag{20}$$

In this work, for the considered precoding algorithms summarized below, we impose the total power constraint (TPC) formulated in (20) to be always true due to common digital transparent payload OBP implementations [27].

1) uP-MMSE: The well known low-complexity MMSE precoder, that has the objective of maximizing the total offered capacity, is deployed using a uniform power allocation, i.e.,:

$$\boldsymbol{Q} = \sqrt{\boldsymbol{P}_{\mathrm{uP}}}\boldsymbol{V}, \tag{21}$$

$$\boldsymbol{V} = \left(\boldsymbol{H}^{\dagger}\boldsymbol{H} + \epsilon \boldsymbol{I}_K\right)^{-1}\boldsymbol{H}^{\dagger}. \tag{22}$$

The unit-norm matrix $\boldsymbol{V} \in \mathbb{C}^{K\times K}$ has the MMSE precoding coefficients such that $\|\boldsymbol{V}\|^2 = K$ and $\epsilon = \frac{K}{P^{\text{tot}}}$ [29] is regularization term. Here, the diagonal power factor matrix $\boldsymbol{P}_{\text{uP}} \in \mathbb{R}^{K\times K}$ has elements $[\boldsymbol{P}_{\text{uP}}]_{k,k} = \frac{P^{\text{tot}}}{K}$ and verifies TPC.

2) wP-MMSE: To account for traffic matching, a power flexibility is added in this algorithm. In particular, the diagonal power factor matrix has elements that utilize the sub-optimal weighted water-filling power allocation solution [38] as in

$$\boldsymbol{Q} = \sqrt{\boldsymbol{P}_{\text{wP}}}\boldsymbol{V}, \tag{23}$$

$$[\boldsymbol{P}_{\text{wP}}]_{k,k} = \max\left(\frac{1}{z_k}[\boldsymbol{w}]_k - \frac{P_{\text{n}}}{\left|\left[\boldsymbol{h}_k^{\dagger}\right]_k[\boldsymbol{q}_k]_k\right|^2}, 0\right). \tag{24}$$

The weights in $\boldsymbol{w} \in \mathbb{R}_{>0}^{K\times 1}$ play the role of the QoS requirements in the form of the user priority where less important users are assigned higher weights and vice-versa. In our analysis, the weights are taken as the inverse of the Shanon-sense required signal-to-noise ratio (SNR), such that

$$[\boldsymbol{w}]_k = \frac{1}{2^{\left(\left[\tilde{\boldsymbol{D}}\right]_k/\text{B}_0\right)} - P_{\text{n}}\text{B}_0}. \tag{25}$$

This way the weights are inversely proportional to each super-user's traffic demand. Furthermore, to satisfy the TPC, the elements of $\boldsymbol{w}$ are scaled by a corresponding scalar $z_k > 0, \forall k \in \mathcal{K}$ as seen in (24).

3) sP-MMSE: Consider the SNR requirements of each user to be represented in the diagonal matrix $\boldsymbol{\Upsilon} \triangleq (\boldsymbol{1}_K \oslash \boldsymbol{w})\boldsymbol{I}_K \in \mathbb{R}^{K\times K}$. Given the MMSE precoding matrix $\boldsymbol{V}$, a method by [39] gives a power minimizing solution $\boldsymbol{p}^{\Pi} \in \mathbb{R}^{K\times 1}$ satisfying the requirements in policy $\Pi \leftrightsquigarrow (\boldsymbol{V}, \boldsymbol{\Upsilon}, P^{\text{tot}})$, using the facts

$$\boldsymbol{p}^{\Pi} = \left(\text{diag}\left(\boldsymbol{\Gamma}^{\Pi}\right) - \boldsymbol{\Upsilon}\left(\boldsymbol{\Gamma}^{\Pi} - \text{diag}\left(\boldsymbol{\Gamma}^{\Pi}\right)\right)^{-1}\boldsymbol{\Upsilon}\boldsymbol{1}_K, \tag{26}$$

$$\boldsymbol{\Gamma}^{\Pi} \triangleq \boldsymbol{V}\boldsymbol{H}\boldsymbol{H}^{\dagger}\boldsymbol{V}, \tag{27}$$

where the matrix $\boldsymbol{\Gamma} \in \mathbb{C}^{K\times K}$ is the interference coupling matrix after applying $\boldsymbol{V}$ [39]. If all elements of $\boldsymbol{p}^{\Pi}$ are positive then a solution given Π is feasible. In this case we denote the *smart* diagonal power factor matrix $\boldsymbol{P}_{\text{sP}}$ as a scaled version of the solution to satisfy the TPC, i.e.:

$$\boldsymbol{Q} = \sqrt{\boldsymbol{P}_{\text{sP}}}\boldsymbol{V}, \tag{28}$$

$$[\boldsymbol{P}_{\text{sP}}]_{k,k} = \frac{1}{z_k}[\boldsymbol{p}^{\Pi}]_k. \tag{29}$$

4) w-MM: Here, the precoder has the goal of maximizing the minimum weighted SINR γ under the TPC, i.e.:

$$\max_{\boldsymbol{Q}} \min_{k\in\mathcal{K}} [\boldsymbol{w}]_k\gamma_k$$
$$\text{subject to } \|\boldsymbol{Q}\|^2 \le P. \tag{30}$$

This precoder achieves a fair system performance and its precoding matrix $\boldsymbol{Q}$ is solved here using the close to optimal convex-concave procedure [21] after converting (30) to a difference-of-convex programming problem.

For $N_{\text{c}} > 0$, the SINR of the u-th user is expressed by[3]

$$\gamma_u = \frac{\left|\boldsymbol{h}_u^{\dagger}\boldsymbol{q}_u\right|^2}{\sum_{j\in\mathcal{C}_{(u)}\setminus\{u\}}\left|\boldsymbol{h}_u^{\dagger}\boldsymbol{q}_j\right|^2 + P_{\text{n}}\frac{\text{B}_0}{N_{\text{c}}}}, \tag{31}$$

where the operator (u) returns the color index $i \in [1, \ldots, N_c]$ of user $u \in \mathcal{C}_i \subseteq \mathcal{K}$ belonging to co-channel group $\mathcal{C}_i$.

B. Precoding With Non-Ideal CSI Estimation

In order to assess the impact of the practical limitations on precoding performance in the proposed beam footprints, we consider the CSI estimation errors (EE) [31] that can be due to non-perfect feeder-link calibrations, on-board signal-to-noise-ratio (SNR) levels non-linearities, and/or EE at the UTs. Consider then the estimated channel $\hat{\boldsymbol{H}}$ at the gateway with a per-beam error vector $\boldsymbol{E} \in \mathbb{C}^{K\times 1}$, which we write as

$$\hat{\boldsymbol{H}} = \tilde{\boldsymbol{H}} + \text{diag}(\boldsymbol{E}). \tag{32}$$

We are interested in the actual performance of a system having a precoding matrix $\hat{\boldsymbol{Q}}$ using an estimated $\hat{\boldsymbol{H}}$ and an instantaneous $\boldsymbol{H}$. The PHY in linear form for such systems is

$$\boldsymbol{y} = \boldsymbol{H}\hat{\boldsymbol{Q}}\boldsymbol{s} + \boldsymbol{n}. \tag{33}$$

According to [30], the non-perfect channel coefficient estimation can be modeled with an additive Gaussian error with a mean μ_E and a variance σ_E^2. These latter EE parameters depend on the statistics of the SNR υ and the signal-to-interference-ratio (SIR) ν experienced in the ideal case for each realization, i.e., $[\boldsymbol{E}]_u \sim \mathcal{CN}(\mu_E(\upsilon_u, \nu_u), \sigma_E^2(\upsilon_u, \nu_u))$.

In general, co-channel users experience mutual interference, expressed for the u-th scheduled user as SIR with

$$\upsilon_u = \frac{|\boldsymbol{h}_u^{\dagger}\boldsymbol{q}_u|^2}{\sum_{j\in\mathcal{C}_{(u)}\setminus\{u\}}|\boldsymbol{h}_u^{\dagger}\boldsymbol{q}_j|^2}. \tag{34}$$

Additionally, the SNR for the u-th user is expressed as

$$\nu_u = \frac{\left|\boldsymbol{h}_u^{\dagger}\boldsymbol{q}_u\right|^2}{P_{\text{n}}\frac{\text{B}_0}{N_{\text{c}}}}. \tag{35}$$

In [30], only $\nu^{\text{dB}} = 10\,\text{dB}$ is considered with a maximum $\upsilon^{\text{dB}} = 16\,\text{dB}$ for channel locking considering synchronization miss-alignments and frequency offsets. Using empirical results from a real PHY chain emulation [32] and assuming carriers to be synchronous in frequency and time, it is envisaged that a possible experience with up to $\upsilon^{\text{dB}} = 21\,\text{dB}$ would allow channel coefficient estimation for a ν^{dB} range up to 14 dB.

V. Simulation Results

In this section, we compare the performance of different HTS system configurations of interest, namely featuring 4FR and FFR with and without DBF. First, we define key performance indicators (KPIs) at the system-level, at the beam-level and at the user-level. We then consider the scenario with the highest global demand (i.e., traffic pattern at 12 h; see

[3]We exploit the same notation of (31) for the *non-precoded* systems using $\boldsymbol{Q} = \sqrt{\boldsymbol{P}_{\text{uP}}}$ to distinguish the uniform power allocation plan in the conventional RRM strategy [5] with $N_{\text{c}}^{\text{4FR}} = 4$.

TABLE I
HTS SYSTEM SPECIFICATIONS

$f_0 = 19.2\,\text{GHz}$	P_{L} same as in [5]
$\text{B}_0 = 428.57\,\text{MHz}$	P_{n} same as in [5]
$G_{\text{RBLP}}^{\text{EP,dBi}} = 51.34\,\text{dBi}$	$P^{\text{max,dB}} = 37\,\text{dB}$
$G_{\text{RX}}^{\text{dB}} = 39.41\,\text{dB}$	$P^{\text{tot,*,dB}} = 32\,\text{dB}$ from $\mathcal{P}^{(2)}$
$(R_s, \rho_s, \phi_s) = (42\,657\,\text{km}, 13^\circ, 0^\circ)$	$\zeta = 0.05$
$A = 120\lambda$	$\gamma_0^{\text{dB}} = 1\,\text{dB}$

Fig. 1) emulated by the TE over Europe [1], [5]. And finally, we focus on the hourly traffic patterns during a one day period.

Similar to [5], [18], [26], we keep a fixed user-link bandwidth B_0 and a fixed number of beams K for a fair comparison. We consider the RBLP based on a satellite system (i.e., *SX*0) covering the Pan-European area, provided by the European Space Agency (ESA). The RBLP has a number $K = 71$ of beams, which we fit to the ITU-R radiation model as described in [5]. We use the minimum required power budget $P^{\text{tot},*}$ from the solution of $\mathcal{P}^{(2)}$. The rest of HTS simulated system parameters are summarized in Table I.

A. Performance Metrics

The channel matrix (2) and correspondingly the performances depend on the selected served super-user positions and PHY changes in time according to a defined scheduling algorithm. Hence, we base our simulations on a large number of channel realizations $N_{\text{MC}} > 0$ with arbitrary user locations (see (3)). This is particularly important to take into account the spatial scheduling effect at the user-level due to DBF.

For each observed traffic pattern and for each considered system configuration, we adopt the DVB-S2X spectral efficiency step function [30] $f_{\text{DVB-S2X}}$ to measure the user-link achievable throughput. This latter is defined for user u in beam k in bps using $R_{u,k} = \frac{\text{B}_0}{N_{\text{c}}} \frac{1}{1+\zeta} f_{\text{DVB-S2X}}(\gamma_u - \gamma_0)$, where γ_0 is the link-margin and ζ is the roll-off factor of the shaping filter. Averaging out the achievable rates over the realizations yields $R_k = \frac{1}{N_{\text{MC}}} \sum_{u=1}^{N_{\text{MC}}} R_{u,k}$, i.e., the offered throughput at beam k. Each system configuration has then a $\text{TOT} = \sum_{k=1}^{K} R_k$. We obtain the UC and EC quantities using

$$\text{BUC}_k = \max\left(\left[\widetilde{\boldsymbol{D}}\right]_k - R_k, 0\right) \tag{36}$$

$$\text{SUC} = \sum_{k=1}^{K} \text{BUC}_k \tag{37}$$

$$\text{BEC}_k = \max\left(R_k - \left[\widetilde{\boldsymbol{D}}\right]_k, 0\right) \tag{38}$$

$$\text{SEC} = \sum_{k=1}^{K} \text{BEC}_k. \tag{39}$$

As a matter of fact, the performance of the system is not only linked to the spectral efficiency, or demand only, but also to the user channel access period in the time domain. This is crucial when analyzing non-uniform user distributions over time and coverage.[4] To capture this temporal dimension, we define an additional KPI highlighting the "channel access": which is the average system satisfaction index (ASSI) for a system observed at t, i.e.:

$$\text{ASSI}^{(t)} \triangleq \frac{1}{KN_{\text{MC}}} \sum_{k=1}^{K} \sum_{u=1}^{N_{\text{MC}}} \min\left(\frac{R_{u,k}^{(t)}}{D_{u,k}^{(t)}}, 1\right). \tag{40}$$

The ASSI is a scalar between 0 and 1. Considering all realisations, a higher ASSI value indicates more satisfaction at the user-level, and vice-versa.

TABLE II
PERFORMANCE OF DIFFERENT CONFIGURATIONS AT THE PEAK TRAFFIC DEMAND SCENARIO. SUC AND SEC ARE IN Gbps WHILE THE ASSI IS DIMENSIONLESS BETWEEN 0 AND 1

KPI/RRM	4FR	uP-MMSE	wP-MMSE	sP-MMSE	wMM
*SX*0	RBLP beampattern (benchmark)				
SUC	20.40	5.86	5.00	5.21	10.50
SEC	1.07	7.43	4.87	4.87	1.23
ASSI	0.83	0.78	0.79	0.79	0.80
*SX*10	Initially targeted ABLP beampattern				
SUC	18.38	4.69	5.66	4.90	6.02
SEC	0	6.52	6.08	5.97	1.16
ASSI	0.95	0.92	0.93	0.92	0.93
*SX*11	Feasible ABLP beampattern with beam gain control				
SUC	17.30	4.50	4.91	4.42	5.87
SEC	0	7.49	7.00	6.91	1.29
ASSI	0.95	0.92	0.93	0.92	0.93
*SX*12	Feasible ABLP beampattern with directivity control				
SUC	17.29	4.28	4.60	4.15	5.40
SEC	0	8.00	7.51	7.47	1.53
ASSI	0.95	0.92	0.93	0.92	0.93

B. Peak Traffic Demand Scenario

Here, we study the scenario of the traffic pattern with the highest global demand equal to 868.96 Gbps and modeled by the TE [1] at $t = 12\,\text{h}$. This scenario emulates 62223 disperse users with heterogeneous demands over the service area (see [5]). The corresponding traffic pattern is shown in Fig. 1.

Before presenting the obtained performance, we provide in Fig. 4 the superimposed beampatterns corresponding to the different system HTS configurations including the ones proposed in Section III. The first subfigure (Fig. 4-a) represents the benchmark beampatterns of a non-DBF system (i.e., *SX*0) with a RBLP. The second subfigure (Fig. 4-b) represents the DBF initial target beampattern design with no practical constraints (i.e., *SX*10). The third subfigure (Fig. 4-c) represents the DBF beampatterns considering the practical constraints after solving $\mathcal{P}^{(1)}$, while the last subfigure (Fig. 4-d) corresponds to the solution of $\mathcal{P}^{(2)}$. The obtained performance results for the above-mentioned configurations are depicted in Table II.

[4] In other words, DBF spatially *schedules* users sharing a TDM frame based on the ABLP. Consider the users in a hot-spot ZOI sharing a beam with a relatively high number of co-channel users. While this seems not favorable given short user-link access time, hot-spot beams compensate the transmission with a higher gain, i.e., received power, and as a results a higher spectral efficiency is attained. In the other situation, cold-spot beams with relatively worse link-budget have lesser users competing to access the channel. This is to be compared with an RBLP, where users in hot-spot ZOI access the channel a fraction of time similar to users in cold-spots, which results in a relatively poorer system performance.

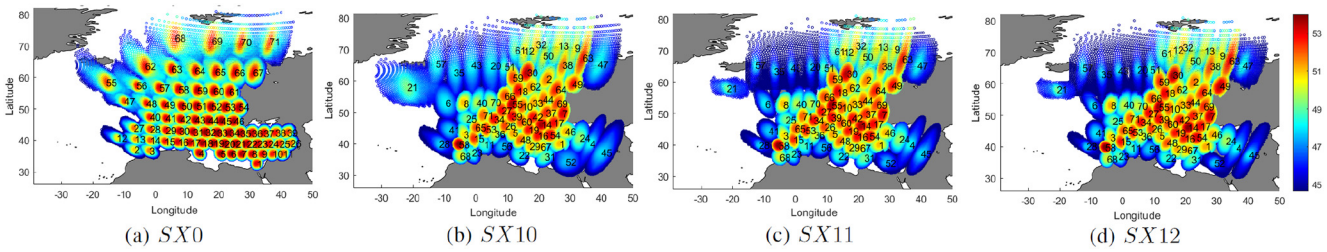

Fig. 4. Beampatterns in dBi of the considered systems at the peak traffic demand scenario ($t = 12$ h).

We start by comparing the performances for the 4FR case for systems with DBF off ($SX0$) and for systems with DBF on ($SX10$). We first notice a 10% improvement in SUC in favor of $SX10$ in comparison to $SX0$ and a negligible SEC for $SX10$ against 1.07 Gbps for $SX0$. In addition, a higher ASSI of 0.95 is observed for $SX10$ as compared to 0.83 for $SX0$. With these results, we have verified that, for 4FR, the expected traffic matching design objective of the ABLP is attained at the system, beam, and user levels.

We now move to the precoded FFR cases. For each of the considered systems, we notice a higher respective TOT for the precoded cases when compared to 4FR. This expected result is reflected by lower SUC in favor of FFR w.r.t. 4FR. More interestingly, using $SX0$, the highest ASSI for FFR is observed with the w-MM precoder with a value of 0.80 which is lower than 0.83 observed for 4FR. This is to be compared with the $SX10$ system, where the ASSI performance of the FFR cases becomes dominant for all precoders, and at least 11% better than a 0.83 ASSI performance. The latter result justifies the joint use of DBF and precoding at the system, beam, and user levels.

We note that different performance and complexity trade-offs are offered by the different precoding algorithms, as detailed in Table II. For example, uP-MMSE trades off UC/EC for ASSI by nature while w-MM behaves oppositely. The selection among the precoders depends on the objective of the designer and available system resources.

We now move to comparing the feasible systems $SX11$ and $SX12$ to the target system $SX10$. We begin with the ASSI KPI. As opposed to $SX10$ that assumes an ideal RF coverage, since $SX11$ and $SX12$ renounce some RF coverage to satisfy the practical constraints, the ASSI is not expected to improve for the feasible systems. However, a significant drop in ASSI would bring the attention to an unfeasibility in either the initial ABLP design or the satisfaction of the practical constraints under power budget $P^{\max}$. From Table II, this unfavorable case is not observed: the same ASSI values are obtained for $SX10$, $SX11$ and $SX12$ for each respective RRM configuration. This result encourages the use of the designed ABLPs, especially in the current highest traffic demand scenario.

In terms of traffic matching performance, when compared to $SX10$, the highly directive feasible beams of $SX11$ and $SX12$ give a more precise SUC and SEC assessment. In the present scenario, for all RRM configurations, $SX12$ outputs a lower SUC and a higher SEC when compared to $SX10$. While, for all RRM configurations, $SX11$ outputs a lower SUC than both $SX10$ and $SX12$, and a lower SEC than $SX10$. Therefore $SX11$ is superior to $SX12$ in this scenario in terms of traffic matching performance. In nuance, we accentuate the fact that solving problem $\mathcal{P}^{(1)}$ executes K times slower than solving problem $\mathcal{P}^{(2)}$ and requires a power seed assumption which we obtain from the solution of $\mathcal{P}^{(2)}$ as explained in Section III-E. In the sequel, we chose to focus on $SX11$ only when referring to feasible DBF systems.

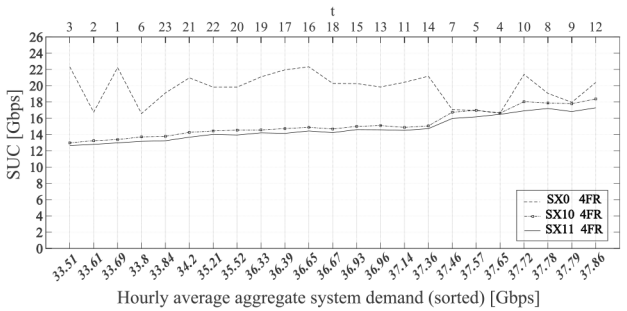

Fig. 5. Over-time SUC performance using 4FR. Compared to without DBF ($SX0$), with DBF ($SX10$), the 4FR SUC performance is better at all instances. Moreover, for all the traffic profiles, the feasible system $SX11$ gives a positive traffic matching gain when compared to $SX10$.

In summary, the analysis in this section encourages the use of DBF for both 4FR and FFR cases. While these appreciations are true for this peak traffic demand scenario, one would want to have a more comprehensive evaluation of the HTS systems performance given the same on-board resources (P^{tot} and B_0) but for time-varying user and traffic distributions. This is tackled in the next section.

C. Over Time Analysis and Trade-Off

In this section, we focus on SUC and ASSI performance of different configurations over-time. The SUC analysis is of interest for the satellite operator to justify the use of DBF given the variable realistic traffic patterns. While the ASSI analysis is essentially a mean of quantifying the coverage losses due to the practical constraints satisfied in the DBF optimization framework in system $SX11$ as compared to $SX10$. Lastly, the impact of non-ideal CSI estimation is added and commented.

1) Traffic Matching Performance (SUC): For systems $SX0$, $SX10$ and $SX11$, the over-time SUC performances (sorted on hourly demand basis) are shown in Fig. 5 for 4FR and in Fig. 6 for FFR. More specifically, subfigures Fig. 6-a, Fig. 6-b, Fig. 6-c, and Fig. 6-d respectively correspond to the uP-MMSE, wP-MMSE, sP-MMSE and w-MM precoders.

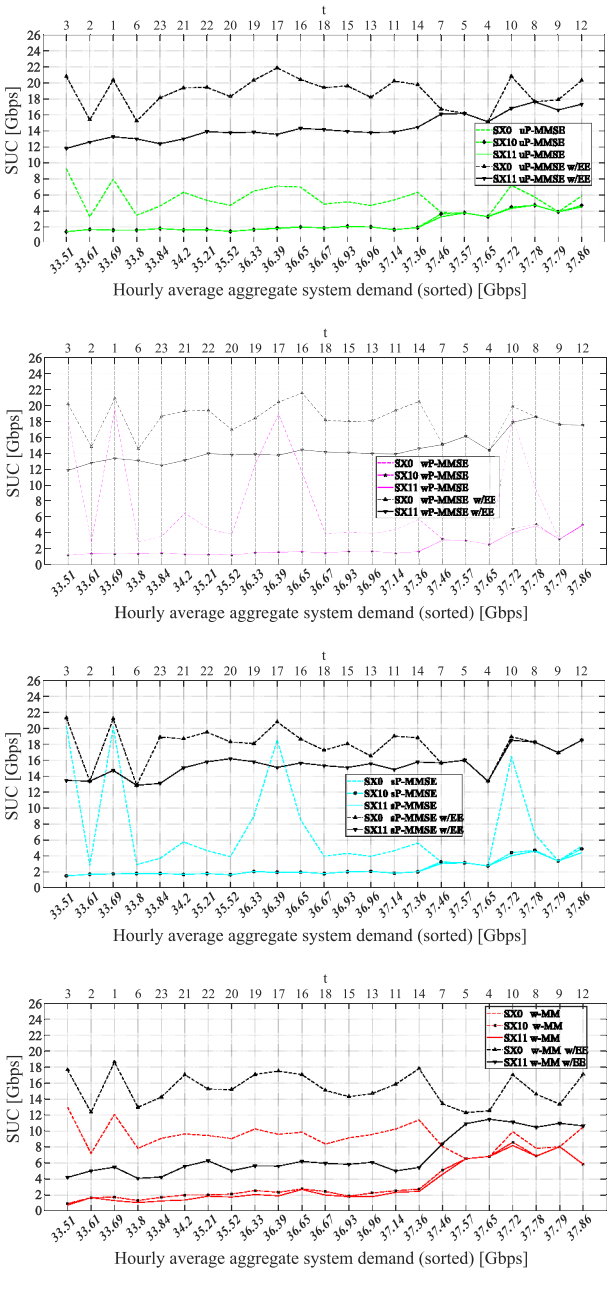

(a) (b) (c) (d)

Fig. 6. Over-time SUC performance using FFR. For the systems *SX*0 and *SX*11, the practical precoders' SUC performance with non-ideal CSI estimation is plotted with respectively dashed and continuous dark lines across the traffic profiles. In these cases, we observe an increase in SUC as compared to the corresponding colored line plots not considering CSI EE.

By admitting the 4FR case as benchmark, we analyse the FFR cases. Starting with the system with DBF off (*SX*0), non-favorable peaks on the SUC are noticed, especially for the wP-MMSE and sP-MMSE precoders (e.g., at instances 3 h, 1 h, 17 h, and 10 h). While with DBF (*SX*10), the SUC performance of the precoders becomes more stable across the traffic profiles. This is particularly true for wP-MMSE and sP-MMSE, where at the mentioned instances, wP-MMSE and sP-MMSE both achieve a lower SUC than uP-MMSE in *SX*10. Hence, the power flexibility (and corresponding complexity) offered by wP-MMSE and sP-MMSE prove to be considerably beneficial when DBF is on.

Regarding the proposed feasible system *SX*11, its traffic matching performance in terms of SUC is not only comparable to the one of system *SX*10, but outperforms it in all cases if we compare each precoder separately. This is a favorable result for the DBF optimization framework elaborated in Section III with highly directive beams, because not only IBI is well modeled, the optimized beampatterns under practical constraints do not sacrifice traffic matching for feasibility.

Moreover, with DBF on, for the FFR cases (as well as for 4FR as seen in Fig. 5), the trend of having more SUC in correlation with a higher system demand is noticed as opposed to the arbitrary behavior with DBF off as seen in Fig. 6. This is because the system is exhausted to output more throughput accordingly given the same on-board resources. This is mostly highlighted for the uP-MMSE and w-MM precoders, where for higher system demands, the SUC gain becomes negligible for a precoded system with DBF on.These results are valuable for the system operator to identify when precoding is needed.

2) FFR SUC Performance Under CSI EE Conditions: We want to see if the latter FFR SUC performances are also true for a realistic end-to-end PHY chain. We do this by considering CSI EE at the gateway using the approach detailed in Section IV-B. The corresponding performances are depicted in black color in Fig. 6.

In this case, we note that on the one hand, using *SX*11, the MMSE-based precoders converge to an SUC performance somewhat close to the one of *SX*0 in the high demand scenarios. On the other hand, the w-MM precoder (Fig. 6-d) achieves considerably lower SUC in *SX*11 (versus *SX*0) for all traffic patterns and under feasible beampatterns even with CSI EE at the gateway. This traffic matching reliability is achieved at the cost of higher complexity compared to MMSE.

3) Channel Access Performance (ASSI): Moving on to the second part of the evaluation, we ultimately aim to quantify the *availability compromise* coming with the feasible DBF system *SX*11 (elaborated in Section III-D) when compared to the initial DBF design in system *SX*10, as well as when DBF is off (i.e., *SX*0). We do this using the ASSI over-time (sorted on hourly demand basis) in Fig. 7 for all the RRM configurations.

We start with DBF off (*SX*0). For this system, 4FR has a higher ASSI (averaged at 0.82) when compared to FFR in most traffic patterns. This is because IBI is mitigated by spectral separation at the expense of lower throughputs as detailed in the previous section. In particular, uP-MMSE, being the least complex, has the lowest ASSI averaged at 0.79 as expected. While w-MM is robust to traffic changes by design and maintains an average ASSI of 0.80.

Now, with DBF enabled, ASSI is superior in *SX*10 w.r.t. *SX*0 for all respective RRM configurations (4FR and FFR). This is an other insight in favor of DBF for both precoded and non-precoded HTS. In particular, as depicted in Fig. 7, the performances of the FFR cases for *SX*10 improve with more complex precoders deployed, i.e., uP-MMSE, sP-MMSE, wP-MMSE then w-MM, in ascending order.

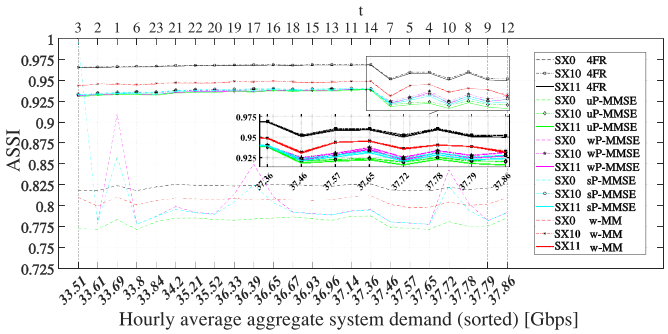

Fig. 7. Over-time ASSI performance. Dashed lines designate $SX0$, solid lines designate $SX10$, and marked dashed lines designate $SX11$. We notice that the performances of $SX11$ are lower bounded by the ones of $SX0$ and tend to achieve the same availabilities as $SX10$, its upper bound.

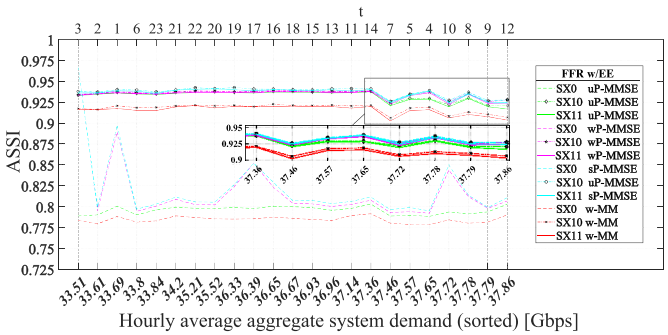

Fig. 8. Over-time ASSI performance using FFR with CSI EE.

For our most important comparison of interest, as expected, $SX10$ with no practical constraints has an upper-bound ASSI across all traffic profiles and RRM configurations when contrasted to $SX11$. This is because the ABLP initial design has no coverage gaps. The same ASSI performance orders in $SX10$ and in $SX11$ are maintained as in $SX0$. The worst case is for the uP-MMSE (in green in Fig. 7) as it is the least complex precoder with lesser flexibility. However, the availability performance of uP-MMSE is not very far in terms of absolute differences in ASSI when comparing $SX11$ to $SX10$. In other words, going from a target to a feasible DBF gives an (over-time) average difference of 0.0022 loss in ASSI. This merit is negligible and reflects a high quality of availability for the proposed feasible DBF system $SX11$.

4) FFR ASSI Performance Under CSI EE Conditions: Let us next evaluate the availability performance of the FFR settings when a CSI EE is experienced at the gateway. In Fig. 8, we present the ASSIs for $SX0$, $SX10$, and $SX11$ using the considered precoders. These ASSI performances are evidently lower than the respective ones shown in Fig. 7 with ideal CSI.

We begin with DBF off ($SX0$). Interestingly, from Fig. 8, in terms of average over-time ASSI, the precoders' performance in ascending order is as follows: w-MM with a 0.77 average, uP-MMSE with 0.79, wP-MMSE with 0.81 and sP-MMSE with 0.82. We notice that wP-MMSE loses its average ASSI placement to sP-MMSE, when compared to the ideal CSI case (Fig. 7). This means that sP-MMSE is the most robust precoder to CSI EE in terms of ASSI.

Moving on to DBF on ($SX10$ and $SX11$), a similar average ASSI performance order is obtained for the precoders when compared to DBF off ($SX0$). However, much superior availability merits are noticed in favor of DBF on (at all instances) thanks to the ABLPs and high directivity.

In particular, for the proposed DBF system $SX11$, across the different traffic profiles, the ASSI performances of the precoders are once again upper-bounded by the respective ones in $SX10$ with ideal RF coverage. More specifically, for the most sensitive (and most complex) precoder, namely w-MM, the average difference in ASSI between the target DBF system $SX10$ and the feasible DBF system $SX11$ is of a magnitude of 0.0021. Here again, this sacrifice is considered a minor cost for the feasibility guarantees of the proposed DBF system.

VI. Conclusion

In this work, the combination of DBF and different precoding techniques are evaluated for a GEO HTS considering irregular and realistic traffic patterns and geotemporal user distributions. A simple and generic DBF optimization framework is proposed to construct feasible and compliant beampatterns under practical constraints and according to a target intelligent ABLP. The DBF framework also determines a minimal power-budget for the system to operate.

Traffic matching and availability guaranteeing performances of the different precoding algorithms with progressive complexity are exhaustively evaluated. Namely, the MMSE precoder, with different schemes featuring an SNR weighting based power allocation, an SIR enhanced smart power allocation and an SINR weighted precoder are implemented and are evaluated in different IBI conditions, including non-ideal CSI estimation at the gateway. Simulation results show that the output practical beampatterns of the DBF optimization framework are highly comparable to the initially designed ones. For the different system configurations, we have also presented methodic trade-off analyses with a major result encouraging the use of DBF for both precoded and non-precoded HTS. A key outcome of our trade-off analyses is that IBI has a constructive role in enabling a better traffic matching for future DBF precoded systems, even when a number of practical constraints are considered.

Appendix
ITU-R S.672 General Radiation Model 2

The *ITU-R S.672 general co-polar model 2* defines the directional gain for *shaped beams* using reference masks and reference angular distances in the spherical orthonormal satellite-centered true-view angles coordinate system (SCS) $(e_\varphi, e_\theta, e_\tau)$. The base e_{φ_k} coincides with the k-th beam reference axis pointing to the nadir of the beam center (ρ_k, ϕ_k), whereas e_θ represents the off-axis angles with respect to the reference and e_τ describes the beam's tilt orientation in the vertical and horizontal directions.

Let the operators $\Omega(m,k)$ and $\Delta(m,k)$ respectively designate the unique point on the boundary of the beamlet ∂B_k and the unique point on the k-th ZOI boundary ∂Z_k in the direction of a point m from the center of the beamlet B_k.

$$G^{\mathrm{dBi}}(m,k)=\begin{cases} G_k^{\mathrm{EP,dBi}}-3\left(\frac{\theta_{m,k}}{\omega(m,k)}\right)^2, & \delta(m,k)<0^\circ \\ G_k^{\mathrm{EP,dBi}}-3-\alpha_0\beta_1\left(\left(1+\frac{\delta(m,k)}{\omega(m,k)}\right)^2-1\right), & 0^\circ\le\delta(m,k)<\alpha_1\omega(m,k) \\ G_k^{\mathrm{EP,dBi}}-\beta_2Ł, & \alpha_1\omega(m,k)\le\delta(m,k)<(\alpha_1+0.5)\omega(m,k) \\ G_k^{\mathrm{EP,dBi}}-\beta_2Ł+2.5\left((\alpha_1+0.5)-\frac{\delta(m,k)}{\omega(m,k)}\right), & (\alpha_1+0.5)\omega(m,k)\le\delta(m,k)<(\alpha_1+4.5)\omega(m,k) \\ \max\left\{G_k^{\mathrm{EP,dBi}}-\beta_2Ł-10+20\ln\left(\frac{(\alpha_1+4.5)\omega(m,k)}{\delta(m,k)}\right),0\right\}, & (\alpha_1+4.5)\omega(m,k)\le\delta(m,k)<(\alpha_1+4.5)\alpha_2\omega(m,k) \\ 0, & (\alpha_1+4.5)\alpha_2\omega(m,k)\le\delta(m,k)\le 90^\circ \end{cases} \tag{41}$$

TABLE III
PAYLOAD SPECIFIC ENHANCEMENT PARAMETERS FOR THE GENERAL BEAM RADIATION TEMPLATE

Parameter	Description
$\alpha_0>0$	Main lobe parameter: defined in function of the scan angle, beam broadening, angular displacement (in both azimuth and elevation planes), A/λ, and radiating element degradation effects due to specific antenna configurations (i.e. focal axes and geometry).
$\alpha_1\triangleq\sqrt{1+\frac{\beta_2Ł-3}{\beta_1\alpha_0}}-1$	Corresponds to a $-\beta_2Ł$ dB level with respect to the EP gain.
$\beta_1>0$	Adjustment factor proportional to the sharpness of the main beam roll-off with a unitary default value, i.e., $\beta_1=1$.
$\beta_2>0$	Adjustment factor proportional to the sidelobe plateau region with a unitary default value, i.e., $\beta_2=1$.

For an elliptic beamlet B_k circumscribing a convex ZOI Z_k with a minimal area, its radiated gain experienced at point m can be expressed in the logarithmic scale as in (41), shown at the top of the page. The measure $\delta(m,k)\triangleq\theta_{m,\Delta(m,k)}=\theta_{m,k}-\theta_{k,\Delta(m,k)}$ approximates the angular distance to a point m from the convex ZOI boundary in a direction normal to the closest polygonal side of Z_k [28]. The measure $\omega(m,k)\triangleq\theta_{k,\Omega(m,k)}\ge 0^\circ$ represents the radial distance from the center of beamlet B_k in the direction of point m intersecting with ∂B_k, i.e., the boundary of beamlet B_k. These two measures depict the directivity of an LSAA by representing the shape of a beam k and its roll-off characteristics.

Specifically, to emphasize the high directive capabilities of emerging LSAA, inside the k-th target service ZOI Z_k (region A corresponding to $\delta(m,k)<0^\circ$ in (41)), we assume an elliptic gain variation [33] with an EP gain at the centroid coordinate of the ZOI similar to (5), that is θ_k the off-boresight angle in the CCS. While outside the ZOI, the different beam gain mask regions (B, C, D, E, F) are considered as depicted in Fig. 2 for continuous off-beam-axis angles (θ) in a direction normal to one side of an arbitrary ZOI. Moreover, the model has adjustable parameters according to the payload architecture specificities which are summarized in Table III.

In (41), the case where $\delta(m,k)<0^\circ$ (region A in Fig. 2) defines the beampattern inside the service zone. Outside the service zone, the beampattern is expressed using the adequate reference regions in [28]. More specifically, the main lobe skirt region corresponds to the case $0^\circ\le\delta(m,k)<\alpha_1\omega(m,k)$ (region B in Fig. 2) The near sidelobe region corresponds to the case $\alpha_1\omega(m,k)\le\delta(m,k)<(\alpha_1+0.5)\omega(m,k)$ (region C in Fig. 2), the intermediate sidelobe region corresponds to the case $(\alpha_1+0.5)\omega(m,k)\le\delta(m,k)<(\alpha_1+4.5)\omega(m,k)$ (region D in Fig. 2), the wide-angle sidelobe region corresponds to the case $(\alpha_1+4.5)\omega(m,k)\le\delta(m,k)<(\alpha_1+4.5)\alpha_2\omega(m,k)$ (region E in Fig. 2), and the far-out sidelobe region corresponds to the case $(\alpha_1+4.5)\alpha_2\omega(m,k)\le\delta(m,k)\le 90^\circ$ (region F in Fig. 2).

ACKNOWLEDGMENT

The authors would like to thank Mr. Puneeth J. Honnaiah for providing us with thoughtful insights in early stages of this work as well as for sharing the codes related to the ABLP proposed in [26].

REFERENCES

[1] H. Al-Hraishawi, E. Lagunas, and S. Chatzinotas, "Traffic simulator for multibeam satellite communication systems," in *Proc. 10th Adv. Satell. Multimedia Syst. Conf. 16th Signal Process. Space Commun. Workshop (ASMS/SPSC)*, Graz, Austria, Oct. 2020, pp. 1–8.

[2] A. I. Perez-Neira, M. A. Vazquez, M. R. B. Shankar, S. Maleki, and S. Chatzinotas, "Signal processing for high-throughput satellites: Challenges in new interference-limited scenarios," *IEEE Signal Process. Mag.*, vol. 36, no. 4, pp. 112–131, Jul. 2019.

[3] O. Kodheli *et al.*, "Satellite communications in the new space era: A survey and future challenges," *IEEE Commun. Surveys Tuts.*, vol. 23, no. 1, pp. 70–109, 1st Quart., 2021.

[4] "SES-17 Advanced DTP." SES. [Online]. Available: www.ses.com/news/ses-17-experienceendless-connectivity (Accessed: Oct. 2021).

[5] H. Chaker, N. Maturo, S. Chatzinotas, H. Chougrani, W. A. Martins, and J. Grotz, "Enablers for matching demand in GEO multi-beam satellites: Dynamic beamforming, precoding, or both?" in *Proc. 38th Int. Commun. Satell. Syst. Conf. (ICSSC)*, Arlington, VA, USA, 2021, pp. 104–111.

[6] G. Cocco, T. de Cola, M. Angelone, Z. Katona, and S. Erl, "Radio resource management optimization of flexible satellite payloads for DVB-S2 systems," *IEEE Trans. Broadcast.*, vol. 64, no. 2, pp. 266–280, Jun. 2018.

[7] J. J. G. Luis, N. Pachler, M. Guerster, I. del Portillo, E. Crawley, and B. Cameron, "Artificial intelligence algorithms for power allocation in high throughput satellites: A comparison," in *Proc. IEEE Aerosp. Conf.*, Big Sky, MT, USA, Mar. 2020, pp. 1–15.

[8] J.-T. Camino, C. Artigues, L. Houssin, and S. Mourgues, "Mixed-integer linear programming for multibeam satellite systems design: Application to the beam layout optimization," in *Proc. Annu. IEEE Syst. Conf.*, Orlando, FL, USA, Apr. 2016, pp. 1–6.

[9] K. Kiatmanaroj, C. Artigues, L. Houssin, and F. Messine, "Frequency allocation in a SDMA satellite communication system with beam moving," in *Proc. IEEE Int. Conf. Commun. (ICC)*, Ottawa, ON, Canada, Jun. 2012, pp. 3265–3269.

[10] M. Takahashi, Y. Kawamoto, N. Kato, A. Miura, and M. Toyoshima, "Adaptive power resource allocation with multi-beam directivity control in high-throughput satellite communication systems," *IEEE Wireless Commun. Lett.*, vol. 8, no. 4, pp. 1248–1251, Aug. 2019.

[11] M. Takahashi, Y. Kawamoto, N. Kato, A. Miura, and M. Toyoshima, "Adaptive multi-beam arrangement for improving throughput in an HTS communication system," in *Proc. IEEE Int. Conf. Commun. (ICC)*, Dublin, Ireland, Jun. 2020, pp. 1–6.
[12] J.-T. Camino, S. Mourgues, C. Artigues, and L. Houssin, "A greedy approach combined with graph coloring for non-uniform beam layouts under antenna constraints in multibeam satellite systems," in *Proc. 7th Adv. Satell. Multimedia Syst. Conf. 13th Signal Process. Space Commun. Workshop (ASMS/SPSC)*, Livorno, Italy, Sep. 2014, pp. 374–381.
[13] B. Liu, C. Jiang, L. Kuang, and J. Lu, "Joint user grouping and beamwidth optimization for satellite multicast with phased array antennas," in *Proc. IEEE Global Commun. Conf. (GLOBECOM)*, Taipei, Taiwan, Dec. 2020, pp. 1–6.
[14] J.-T. Camino, C. Artigues, L. Houssin, and S. Mourgues, "Linearization of Euclidean norm dependent inequalities applied to multibeam satellites design," *Comput. Optim. Appl.*, vol. 73, no. 2, pp. 679–705, Jun. 2019.
[15] P. Angeletti and J. L. Cubillos, "Traffic balancing multibeam antennas for communication satellites," *IEEE Trans. Antennas Propag.*, vol. 69, no. 12, pp. 8291–8303, Dec. 2021.
[16] J.-T. Camino, C. Artigues, L. Houssin, and S. Mourgues, "MILP formulation improvement with k-means clustering for the beam layout optimization in multibeam satellite systems," *Comput. Ind. Eng.*, vol. 158, Aug. 2021, Art. no. 107228.
[17] M. Takahashi, Y. Kawamoto, N. Kato, A. Miura, and M. Toyoshima, "DBF-based fusion control of transmit power and beam directivity for flexible resource allocation in HTS communication system toward B5G," *IEEE Trans. Wireless Commun.*, vol. 21, no. 1, pp. 95–105, Jan. 2022.
[18] G. Taricco and A. Ginesi, "Precoding for flexible high throughput satellites: Hot-spot scenario," *IEEE Trans. Broadcast.*, vol. 65, no. 1, pp. 65–72, Mar. 2019.
[19] V. Icolari, S. Cioni, P.-D. Arapoglou, A. Ginesi, and A. Vanelli-Coralli, "Flexible precoding for mobile satellite system hot spots," in *Proc. IEEE Int. Conf. Commun. (ICC)*, Paris, France, May 2017, pp. 1–6.
[20] A. Guidotti and A. Vanelli-Coralli, "Design trade-off analysis of precoding multi-beam satellite communication systems," in *Proc. IEEE Aerosp. Conf.*, Big Sky, MT, USA, 2021, pp. 1–12.
[21] A. Bandi, B. Shankar M. R, S. Chatzinotas, and B. Ottersten, "A joint solution for scheduling and precoding in multiuser MISO downlink channels," *IEEE Trans. Wireless Commun.*, vol. 19, no. 1, pp. 475–490, Jan. 2020, doi: 10.1109/TWC.2019.2946161.
[22] G. Zheng, S. Chatzinotas, and B. Ottersten, "Generic optimization of linear precoding in multibeam satellite systems," *IEEE Trans. Wireless Commun.*, vol. 11, no. 6, pp. 2308–2320, Jun. 2012.
[23] A. I. Aravanis, B. Shankar M. R, P.-D. Arapoglou, G. Danoy, P. G. Cottis, and B. Ottersten, "Power allocation in multibeam satellite systems: A two-stage multi-objective optimization," *IEEE Trans. Wireless Commun.*, vol. 14, no. 6, pp. 3171–3182, Jun. 2015, doi: 10.1109/TWC.2015.2402682.
[24] T. S. Abdu, S. Kisseleff, E. Lagunas, and S. Chatzinotas, "Flexible resource optimization for GEO multibeam satellite communication system," *IEEE Trans. Wireless Commun.*, vol. 20, no. 12, pp. 7888–7902, Dec. 2021.
[25] P. Angeletti and R. De Gaudenzi, "Heuristic radio resource management for massive MIMO in satellite broadband communication networks," *IEEE Access*, vol. 9, pp. 147164–147190, 2021.
[26] P. J. Honnaiah, N. Maturo, S. Chatzinotas, S. Kisseleff, and J. Krause, "Demand-based adaptive multi-beam pattern and footprint planning for high throughput GEO satellite systems," *IEEE Open J. Commun. Soc.*, vol. 2, pp. 1526–1540, 2021.
[27] B. Shankar, M. E. Lagunas, S. Chatzinotas, and B. Ottersten, "Precoding for satellite communications: Why, how and what next?" *IEEE Commun. Lett.*, vol. 25, no. 8, pp. 2453–2457, Aug. 2021.
[28] *Satellite Antenna Radiation Pattern for Use as a Design Objective in the Fixed-Satellite Service Employing Geostationary Satellites*, Rec. ITU-R S.672-4, Int. Telecommun. Union, Geneva, Switzerland, 1997.
[29] D. Christopoulos, S. Chatzinotas, G. Zheng, J. Grotz, and B. Ottersten, "Linear and nonlinear techniques for multibeam joint processing in satellite communications," *EURASIP J. Wireless Commun. Netw.*, vol. 2012, no. 1, p. 162, May 2012, doi: 10.1186/1687-1499-2012-162.
[30] "Implementation guidelines for the second generation system for broadcasting, interactive services, news gathering and other broadband satellite applications; part 2 S2 extensions (DVB-S2X)," ETSI, Sophia Antipolis, France, Rep. TR 102 376-2 V1.2.1, 2015.
[31] A. Tato, S. Andrenacci, E. Lagunas, S. Chatzinotas, and C. Mosquera, "Link adaptation and SINR errors in practical multicast multibeam satellite systems with linear precoding," *Int. J. Satell. Commun. Netw.*, vol. 40, no. 1, pp. 48–66, 2022.
[32] "OPTIMUS." [Online]. Available: wwwen.uni.lu/snt/research/sigcom/projects/optimusoptimizedtransmissiontechniquesforsatcomunicast interactivetraffic (Accessed: Jan. 2022).
[33] G. Maral, M. Bousquet, and Z. Sun, "The communication payload," in *Satellite Communications Systems : Systems, Techniques and Technology*, 6th ed. Hoboken, NJ, USA: Wiley, 2020.
[34] T. Wigren, "A polygon to ellipse transformation enabling fingerprinting and emergency localization in GSM," *IEEE Trans. Veh. Technol.*, vol. 60, no. 4, pp. 1971–1976, May 2011.
[35] *Chapter VI—Provision for Services and Stations. Article 22: Space Services, Radio Regulations Articles*, vol. 1, ITU, Geneva, Switzerland, 2020, pp. 291–311.
[36] *Maximum Permissible Values of Power Flux-Density at the Surface of the Earth Produced by Satellites in the Fixed-Satellite Service Using the Same Frequency Bands Above 1 GHz as Line-of-Sight Radio-Relay Systems*, Rec. ITU-R SF.358-5, Int. Telecommun. Union, Geneva, Switzerland, Oct. 1995.
[37] S. J. Orfanidis, *Electromagnetic Waves and Antennas*. New Brunswick, NJ, USA: Sophocles J. Orfanidis, 2016.
[38] E. Björnson, "Optimal resource allocation in coordinated multi-cell systems," *Found. Trends Commun. Inf. Theory*, vol. 9, nos. 2–3, pp. 113–381, 2013.
[39] H. Boche and M. Schubert, "Theoretical and experimental comparison of optimisation criteria for downlink beamforming," *Eur. Trans. Telecommun.*, vol. 12, no. 5, pp. 417–426, Sep./Oct. 2001.

Haythem Chaker (Graduate Student Member, IEEE) received the State Engineering degree (Dipl.-Ing.) in computer networks and telecommunications from the National Institute of Applied Sciences and Technology, Tunisia, in 2019, and the M.Res. degree in information processing and complexity of living systems from the National Engineering School of Tunis, Tunisia, in co-graduation with the M.Sc. degree in mathematics and computer science from Paris University, France. In 2020, he joined the Signal Processing and Satellite Communications Research Group with SnT, University of Luxembourg as a Ph.D. candidate. His research interests are in wireless systems prototyping with focus on dynamic beamforming design and optimization through the use of new digital signal processing techniques and hardware demonstrations.

Houcine Chougrani received the State Engineering degree in electronics from École Nationale Polytechnique Algiers, Algeria, in 2011, the M.Sc. degree in signal processing from Paul Sabatier University, Toulouse, France, in 2012, and the Ph.D. degree in information technology from École Telecom Bretagne, Brest, France, in 2016. From 2017 to 2018, he was a Research and Development Engineer with the Department of Telecommunication, Airbus Defence and Space, where he worked on the design of communication protocols for satellite payloads both on the system and physical layer levels. From 2018 to 2019, he was a Research and Development Engineer with OQ Technology, where he worked on the integration of the IoT protocol for satellite communication. In 2019, he joined SnT, University of Luxembourg, as a Research Associate and where he is currently a Research Scientist. His research interests include development and implementation of advanced techniques for both terrestrial and satellite communication especially the 3GPP-based protocols.

Wallace A. Martins (Senior Member, IEEE) received the Electronics Engineer degree and the M.Sc. and D.Sc. degrees in electrical engineering from the Federal University of Rio de Janeiro (UFRJ), Rio de Janeiro, Brazil, in 2007, 2009, and 2011, respectively. He was a Research Visitor with the University of Notre Dame, USA, in 2008; Université de Lille 1, France, in 2016; and Universidad de Alcalá, Spain, in 2018. Since 2013, he has been with the Department of Electronics and Computer Engineering (DEL/Poli) and Electrical Engineering Program (PEE/COPPE), UFRJ, where he is currently a Tenured Associate Professor (on leave). He was an Academic Coordinator and the Deputy Department Chairman (DEL/Poli) from 2016 to 2017 with UFRJ. He is currently a Research Scientist working with the SnT, University of Luxembourg. His research interests include the fields of digital signal processing, especially adaptive signal processing and graph signal processing, as well as telecommunications, with focus on equalization and precoding for terrestrial and non-terrestrial (satellite) wireless communications. He was a recipient of the Best Student Paper Award from EURASIP at EUSIPCO-2009, Glasgow, Scotland, the 2011 Best Brazilian DSc Dissertation Award from Capes, and the Best Paper Award at SBrT-2020, Florianópolis, Brazil. He is a member (Associate Editor) of the Editorial Board for the IEEE SIGNAL PROCESSING LETTERS.

Symeon Chatzinotas (Senior Member, IEEE) received the M.Eng. degree in telecommunications from the Aristotle University of Thessaloniki, Thessaloniki, Greece, in 2003, and the M.Sc. and Ph.D. degrees in electronic engineering from the University of Surrey, Surrey, U.K., in 2006 and 2009, respectively. He is currently a Full Professor/Chief Scientist I and the Head of the SIGCOM Research Group with SnT, University of Luxembourg. He was a Visiting Professor with the University of Parma, Italy, and he was involved in numerous Research and Development Projects for the National Center for Scientific Research Demokritos, the Center of Research and Technology Hellas, and the Center of Communication Systems Research, University of Surrey. He has coauthored more than 400 technical papers in refereed international journals, conferences, and scientific books. He was a co-recipient of the 2014 IEEE Distinguished Contributions to Satellite Communications Award and the CROWNCOM 2015 Best Paper Award and the 2018 EURASIC JWCN Best Paper Award. He is currently in the editorial board of the IEEE OPEN JOURNAL OF VEHICULAR TECHNOLOGY and the *International Journal of Satellite Communications and Networking*.

Joel Grotz (Member, IEEE) received the M.Sc. (Dipl.-Ing.) degree in electrical engineering from the University of Karlsruhe, Germany, the Diplome d'Etudes Approfondies degree from the Grenoble Institute of Technology (INPG), France, in 1999, and the Ph.D. degree from KTH, Stockholm, in 2008. He has worked as a Satellite Communications Engineer with SES from 2000 to 2012 and since 2016, in different roles, among which the development of satellite broadband systems, satellite payload responsible on procurement and system design for GEO and MEO high throughput satellite systems, and SES-17 and O3b mPOWER in particular. He is currently leading the development of dynamic resource management of novel flexible satellite systems. From 2012 to 2015, he was with Newtec Cy, Belgium (currently STE iDirect) working on modem system development and end-to-end communication systems for satellite networks. His current research interests include novel transmission techniques for satellite communications, resource management in communication satellite constellations, and antenna array technologies.